ACS NANO

www.acsnano.org

ARTICLE

Direct Measurement of Folding Angle and Strain Vector in Atomically Thin WS_2 Using Second-Harmonic Generation

Ahmed Raza Khan, Boqing Liu, Tieyu Lü, Linglong Zhang, Ankur Sharma, Yi Zhu, Wendi Ma, and Yuerui Lu*

Cite This: *ACS Nano* 2020, 14, 15806−15815

Read Online

ACCESS | Metrics & More | Article Recommendations | Supporting Information

ABSTRACT: **Structural engineering techniques such as local strain engineering and folding provide functional control over critical optoelectronic properties of 2D materials. Local strain engineering at the nanoscale level is practically achieved *via* permanently deformed wrinkled nanostructures, which are reported to show photoluminescence enhancement, bandgap modulation, and funneling effect. Folding in 2D materials is reported to tune optoelecronic properties *via* folding angle dependent interlayer coupling and symmetry variation. The accurate and efficient monitoring of local strain vector and folding angle is important to optimize the performance of optoelectronic devices. Conventionally, the accurate measurement of both strain amplitude and strain direction in wrinkled nanostructures requires the combined usage of multiple tools resulting in manufacturing lead time and cost. Here, we demonstrate the usage of a single tool, polarization-dependent second-harmonic generation (SHG), to determine the folding angle and strain vector accurately and efficiently in ultrathin WS_2. The folding angle in trilayer WS_2 folds exhibiting 1−9 times SHG enhancement is probed through variable approaches such as SHG enhancement factor, maxima and minima SHG phase difference, and linear dichroism. In compressive strain induced wrinkled nanostructures, strain-dependent SHG quenching and enhancement is observed parallel and perpendicular, respectively, to the direction of the compressive strain vector, allowing us to determine the local strain vector accurately using a photoelastic approach. We further demonstrate that SHG is highly sensitive to band-nesting-induced transition (C-peak), which can be significantly modulated by strain. Our results show SHG as a powerful probe to folding angle and strain vector.**

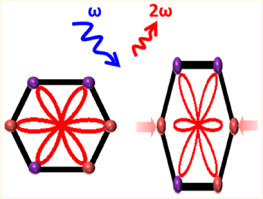

KEYWORDS: *second-harmonic generation (SHG), WS_2, strain, folds, 2D materials*

Two-dimensional (2D) layered semiconductor materials such as transition metal dichalcogenides (TMDs) have received tremendous attention due to their interesting optoelectronic properties and potential applications in electronic devices.[1−10] Tuning the optoelectronic properties of these materials is important for the optimum device performance.[11−20] Therefore, researchers have used various ways to tune the properties of 2D materials such as structural engineering,[21−23] defect engineering,[24] and doping.[25]

Structural engineering of 2D materials provides an exciting platform to tailor the material's properties through modification in the lattice structure. For example, a 2D graphene sheet, a zero-bandgap structure, is rolled to form carbon nanotubes with a tunable bandgap depending on the rolling angle. Armchair nanotubes are metallic structures, whereas zigzag nanotubes show semiconducting properties with an open bandgap.[26−28] Modulation in electronic structure and PL properties is reported through twisting angle modification in TMD heterostructures.[29−31]

Strain engineering[32,33] and folding[34] are two important types of structural engineering techniques to tune optoelectronic properties. For instance, strain engineering is shown to reduce the carrier effective mass and modify the valley structure of atomically thin MoS_2, thus leading to an increase in its career mobility.[35−42] Local strain engineering at the nanoscale level is practically achieved *via* permanently deformed wrinkled nanostructures, which are reported to change the local confinement potential of excitons,[21] modify the bandgap,[21] enhance PL,[43] and improve conductivity.[33] Folding in 2D materials is reported to tune optoelectronic properties *via* folding angle dependent interlayer coupling and symmetry variation. Folded nanostructures of MoS_2 are reported to tune PL intensity due to modulation in interlayer coupling.[34] Both strain engineering and folding provide an effective way to tune

Received: August 17, 2020
Accepted: November 2, 2020
Published: November 12, 2020

Downloaded via AUSTRALIAN NATL UNIV on March 11, 2021 at 13:05:47 (UTC).
See https://pubs.acs.org/sharingguidelines for options on how to legitimately share published articles.

© 2020 American Chemical Society

https://dx.doi.org/10.1021/acsnano.0c06901
ACS Nano 2020, 14, 15806−15815

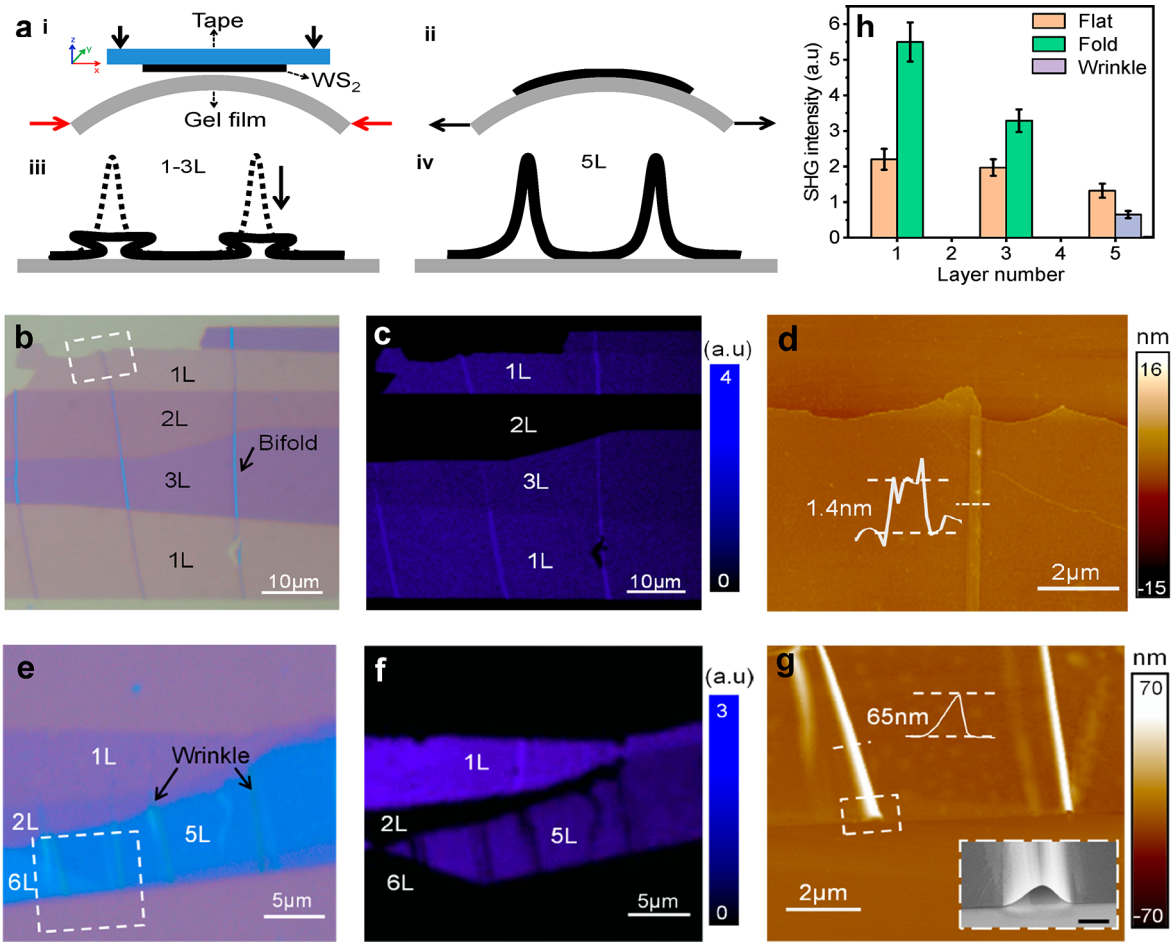

Figure 1. Differentiation of wrinkled and fold nanostructures by SHG. (a) Schematic diagram of the fabrication process of a buckled WS_2 sample. (b) Optical microscopic image of a 1−3L WS_2 sample fabricated by the process described in (a), showing the formation of folds due to collapse of wrinkles. (c) SHG intensity mapping of the region shown in (b). The mapping shows SHG enhancement on 1L and 3L folded regions. (d) AFM topography image of the region marked by the white dashed rectangle in (b). (e) Optical microscopic image of a 5−6L buckled WS_2 sample showing strained wrinkles on 5L and 6L. (f) SHG intensity mapping of the region shown in (e). The SHG mapping shows reduction in SHG on 5L wrinkles. (g) AFM topography image of the region marked by the white dashed rectangle in (e). Inset shows SEM of the wrinkle's profile. (h) A stat-plot showing the SHG response for flat, folded (1L and 3L), and strained wrinkled (5L) regions for ultrathin WS_2. Histogram shows the SHG intensity response, with uncertainties indicated by the error bars. The light brown, green, and light blue rectangles indicate the SHG intensity measurements for flat, folded, and wrinkled regions, respectively. All the measurements are taken at 900 nm laser excitation.

optoelectronic properties and improve the performance of optoelectronic devices; therefore, there is a need of full assessment of local strain vector and folding parameters to utilize their full potential.

Conventionally, determination of both strain amplitude and direction in wrinkled nanostructures requires a combination of multiple tools. For instance, researchers use atomic force microscopy (AFM) and Raman spectroscopy to measure the strain amplitude on strain-induced wrinkles,[21] whereas electron/neutron microscopy is used to determine the relation of strain direction to lattice structure.[44] Recently, optical second-harmonic generation (SHG) has been shown to probe the crystallographic orientation, lattice symmetry, and stacking order of noninversion symmetric 2D materials such as odd layers of TMDs, hBN, and group IV monochalcogenides.[45−48] Because SHG intensity is very sensitive to the structural configurations of 2D materials, it is, in principle, feasible to employ SHG to monitor folding and straining in 2D materials.

Here, we have used polarization-dependent SHG as a single tool to probe folding angle and strain vector precisely in atomically thin tungsten disulfide (WS_2). The folding angle in trilayer WS_2 folds exhibiting 1−9 times SHG enhancement is probed through variable approaches such as SHG enhancement factor, maxima and minima SHG phase difference, and linear dichroism. We find strain-dependent SHG quenching and enhancement, parallel and perpendicular, respectively, to the direction of the compressive strain vector. However, strain angle dependent total SHG (without polarizer) remains constant, which allows us to find the local strain vector accurately using the photoelastic effect. We find SHG to be very sensitive to C-exciton and can be tuned through strain modification. Our results show SHG as a powerful tool to probe both folding angle and strain vector in atomically thin TMDs.

RESULTS AND DISCUSSIONS

In this work, we have used mechanical buckling of the flexible substrate to obtain folds[33,34] (1−3L) and strained wrinkles[21] (5−6L) in atomically thin WS_2. The details of the fabrication method are shown in Figure 1a and are given in the Methods section and in Supporting Information S1. Optical microscopic

https://dx.doi.org/10.1021/acsnano.0c06901
ACS Nano 2020, 14, 15806−15815

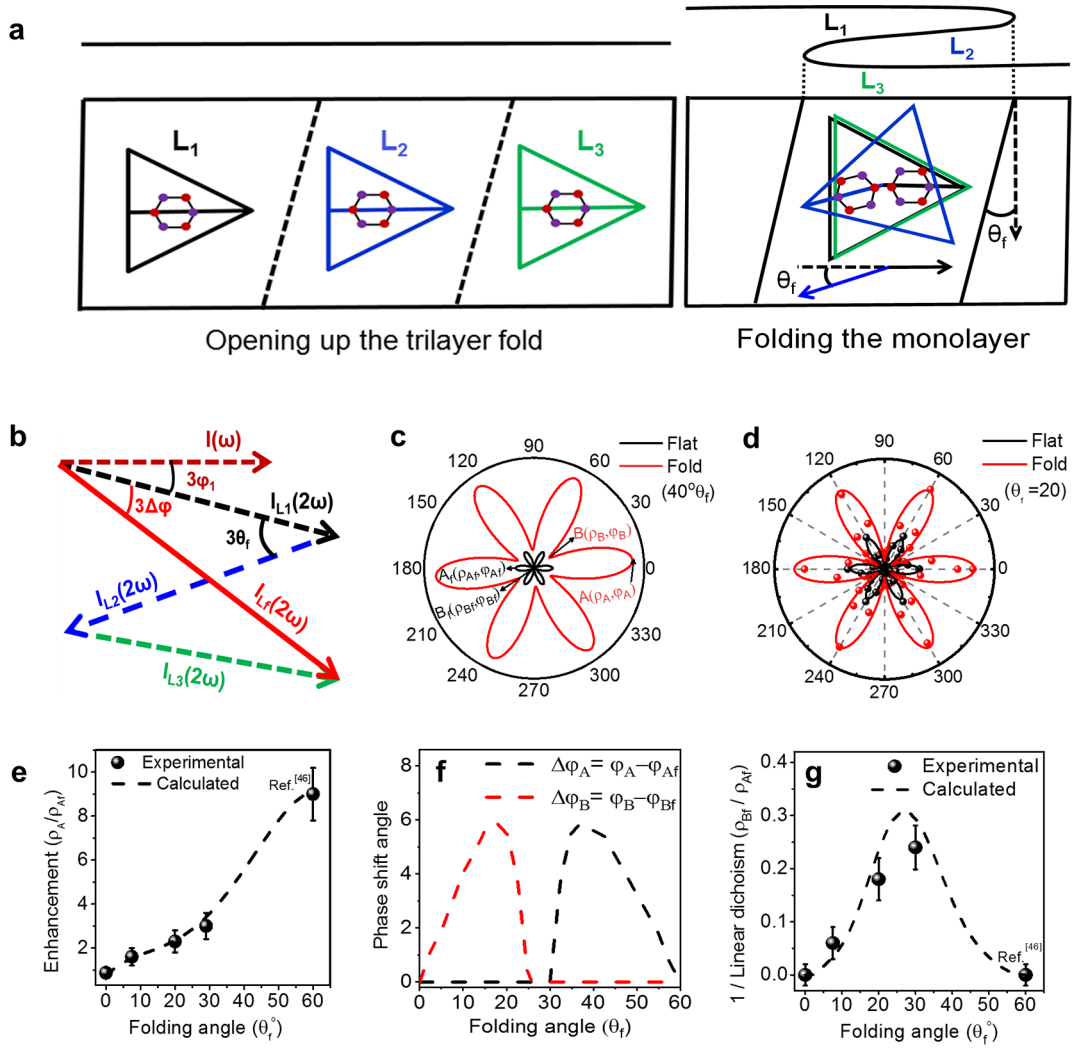

Figure 2. Engineering SHG through folding of atomically thin TMDs. (a) Schematic illustration for the stacking of layers in a trilayer fold (1L +1L+1L). The top (layer 1) and bottom layer (layer 3) are parallel to each other, whereas the armchair direction of middle layer (layer 2) makes an angle of (180+θ_f) with the armchair direction of the top and bottom layer. [The lines (black, blue, and green) bisecting the triangles (black, blue, and green) show the armchair direction]. (b) Vector superposition of the SH fields from the layer of the fold, where $I_{L1}(2\omega)$ (black line), $I_{L2}(2\omega)$ (blue line), and $I_{L3}(2\omega)$ (green line) are the SH wave vectors from L_1, L_2, and L_3, respectively, $I(\omega)$ (brown line) is the laser wave vector, and $I_{Lf}(2\omega)$ is the resultant SH wave vector from the fold. $3\varphi_1$ is the phase shifting angle between input linearly polarized laser and $I_{L1}(2\omega)$, whereas $3\Delta\varphi$ is the phase shifting angle between $I_{L1}(2\omega)$ and $I_{Lf}(2\omega)$. (c) Calculated SHG $I_{\parallel}(2\omega)$ polar response for 1L flat and fold (40° θ_f). $A(\rho_A, \varphi_A)$ is the maximum SHG (ρ_A) amplitude point for the fold with φ_A(degrees) angle from 0°, whereas $B(\rho_B, \varphi_B)$ is the minimum SHG (ρ_B) amplitude point for the fold with φ_B(degrees) angle from 0°. $A_f(\rho_{Af}, \varphi_{Af})$ and $B_f(\rho_{Bf}, \varphi_{Bf})$ represent the maximum and minimum point of the flat region. (d) Experimental investigation of polarization-resolved SHG $I_{\parallel}(2\omega)$ intensity pattern for 1L flat and folded WS_2. Continuous lines are the fitted plots, whereas symbols are experimental data points. (e) Folding angle dependence of SHG enhancement for fold, where enhancement = ρ_A/ρ_{Af}. Shinde *et al.*[46] and Mervin Zhao *et al.*[56] showed experimentally 9 times SHG enhancement in vertically stacked "AAA configuration" and 3R of TMDs, respectively (which is equivalent to a 60° folding angle in the trilayer fold). Reprinted in part with permission under a Creative Commons License from ref 46. Copyright 2018, Springer Nature. (f) The folding angle dependence of SHG phase shift angle (degrees). (g) Folding angle dependence of (linear dichroism)$^{-1}$ where (linear dichroism)$^{-1}$ = ρ_{Bf}/ρ_{Af}. Shinde *et al.*[46] and Jia Shi *et al.*[54] performed polarization-dependent SHG of vertically stacked "AAA configuration" and 3R of TMDs, respectively (equivalent to a 60° folding angle in a trilayer fold). Dashed line is the calculated response, whereas spherical symbols are the experimental data points. Error bars represent the range of error in the measured values. Reprinted in part with permission under a Creative Commons License from ref 46. Copyright 2018, Springer Nature.

images of folds (1−3L) are shown in Figure 1b. Phase shifting interferometry (PSI) is employed to identify the layer number.[13,16,49,50] The wrinkles in 1−3L WS_2 collapse, forming folds due to reduced bending rigidity.[33] As a result, the folds lose their strain with a small/negligible strain left in the folds. This effect is illustrated through negligible shift in PL peak positions between flat and folded TMDs,[34] whereas a considerable shift in PL peak positions is reported in strain-induced MoS_2 wrinkles.[21]

We have used a 900 nm laser excitation confocal light microscope for SHG mapping (450 nm) of flat and folded regions of 1−3L WS_2 as shown in Figure 1c (see Methods section for more details). Odd layers, *i.e.*, 1L, 3L, and 5L, show SHG signal due to non-centrosymmetric structure, whereas even layer numbers do not show SHG signal due to centrosymmetric structure, which is consistent with the previous studies.[48,51] For SHG-folded regions, a multiplying factor is

https://dx.doi.org/10.1021/acsnano.0c06901
ACS Nano 2020, 14, 15806−15815

added in the measurements because the width of folds is smaller than the laser spot diameter (see Section S2 in the Supporting Information for more details). Interestingly, a significantly higher SHG response (~2−3 times) from folded regions is observed as compared to flat regions, as shown in Figure 1c. Power-dependent SHG on flat, folded, and wrinkled regions is performed to confirm if the photons collected are SH photons. The corresponding SHG signal intensity is drawn with excitation power on a log scale. A fitted value of ~2 on a log scale for power *vs* SHG intensity confirms the collected photons as SH photons (Figure S3).[52−54] An AFM investigation shows that the height differences measured on the 1L, 2L, and 3L folds of WS_2 are found to be 1.4 ± 0.5, 2.8 ± 0.5, and 4.2 ± 1 nm, respectively (Figure 1d and Figure S4). These values match the height of 2L, 4L, and 6L WS_2 very well as the thickness of a single layer is evaluated around 0.7 nm,[55] which confirms the bifold formation (such as trilayer fold or 1L+1L+1L on 1L WS_2) in 1−3L WS_2. An SHG investigation of 5L wrinkles shows a drop in SHG as compared to flat 5L (Figure 1f), which will be explained later. An AFM investigation of 4−6L wrinkles reveals a rapid increase in the height (~50−70 nm) as shown in Figure 1g and Figure S4. The wrinkle-like curvature in the scanning electron microscopy (SEM) examination confirms that wrinkles maintain their curvature in ≥4L WS_2. (Figure 1g).

In the previous section, we showed SHG enhancement on folds. The SH response from the fold can be modeled by the vector superposition of all the layers of the fold, which is explained here. Let us consider the case of a trilayer fold (1L+1L+1L) on 1L WS_2. Opening up of the 1L fold shows that the top layer of the fold (designated as L_1 in Figure 2a) is parallel to the bottom layer (L_3), which implies the armchair direction of L_1 (shown as the black line bisecting the hexagonal WS_2 and black triangle in L_1) is parallel to the armchair direction of L_3 (green bisecting line), whereas the armchair direction of the mid-layer L_2 (blue bisecting line) of the fold makes an angle of $180°+\theta_f$ with the armchair direction of L_1 and L_3. These considerations make the trilayer fold different from artificially stacked layers, which may be oriented at any angle. 1L WS_2 belongs to D_{3h} symmetry; therefore, it shows a 6-fold polar SH response as follows:[48]

$$I_{\parallel}(2\omega) \propto cos^2\, 3\varphi \tag{1}$$

where $I_{\parallel}(2\omega)$ is the SHG intensity for parallel polarization (*i.e.*, the polarizer is parallel to the direction of the polarization component of the incident laser) and φ is the azimuthal angle between the polarized incident laser and the armchair direction.[47,48] SHG intensity becomes maximum when the incident laser polarization is parallel to the armchair direction.[48] For our folding case, $I_{L1} = I_{L3} \propto \cos^2 3\varphi_1$ and $I_{L2} \propto \cos^2 3(\varphi_1 + 180 + \theta_f)$ where $I_{L1}(2\omega)$, $I_{L2}(2\omega)$, and $I_{L3}(2\omega)$ are the SHG wave vector responses from L_1, L_2, and L_3 of the fold. Hsu *et al.*[45] reported that the SH wave vector from two stacked layers (I_s) under parallel polarization can be found by the vector superposition of SH wave vectors from two individual layers as follows:

$$I_{s\parallel}(2\omega) \propto I_a + I_b + 2\sqrt{(I_a I_b)}\cos 3(\theta) \tag{2}$$

where θ is the stacking angle between the armchair directions of a and b. Thus, SHG response from the fold can be solved by the vector superposition of the SHG response coming from the individual layers of the fold, *i.e.*, $I_{L1}(2\omega)$, $I_{L2}(2\omega)$, and $I_{L3}(2\omega)$ as shown in Figure 2b.

In the case of our trilayer fold, this can be done by the vector addition of two entities first ($I_{L1}(2\omega)$ and $I_{L2}(2\omega)$) to find their resultant $I_{L12}(2\omega)$ where $\theta = 180 + \theta_f$) and then adding this resultant vector, *i.e.*, $I_{L12}(2\omega)$ to the third entity vector ($I_{L3}(2\omega)$) to get the overall resultant vector $I_{Lf}(2\omega)$ where $I_{Lf}(2\omega)$ is the SH wave vector from the fold. φ_1 is the azimuthal angle between the incident laser polarization component and the armchair direction of $I_{L1}(2\omega)$, whereas $3\Delta\varphi$ is the phase shifting angle between $I_{L1}(2\omega)$ and $I_{Lf}(2\omega)$ as demonstrated in Figure 2b. Using the above scheme, the angular SHG response of the folded region $[I_{Lf}(2\omega)]$ with $\theta_f = 40°$ is calculated as shown in Figure 2c, where $A(\rho_A, \varphi_A)$ is the maximum amplitude point of SHG (ρ_A) for the fold with a φ_A(degrees) angle from horizontal (0°), whereas $B(\rho_B, \varphi_B)$ is the minimum SHG (ρ_B) amplitude point for the fold with a φ_B(degrees) angle from horizontal. $A_f(\rho_{Af}, \varphi_{Af})$ and $B_f(\rho_{Bf}, \varphi_{Bf})$ represent the maximum and minimum points of the flat region. Here, φ_{Af} and φ_{Bf} represent the AC (armchair) direction at 0° and the ZZ (zigzag) direction at 30° because we are using parallel polarization for SHG.

In order to experimentally investigate the polarization-dependent SHG response of the folded region, we put a polarizer in between the sample and the spectrometer in such a position that the polarization component of the SH radiation is parallel to the polarization state of the incident laser (900 nm), *i.e.*, parallel polarization of SHG (see the Methods section for more details). We get an enhanced (~2.6) SHG polar response from the folded region ($\theta_f = 20°$) along the armchair direction as demonstrated in Figure 2d (see Supporting Information Section S5 for folding angle determination). As the folding angle is expected to tune SHG intensity coming from the fold, we calculate the SHG enhancement factor = ρ_A/ρ_{Af} as indicated by the dashed line as shown in Figure 2e. The calculated angular SHG response shows 1 to 9 times SHG enhancement as θ_f goes from 0° to 60°. The experimental results are found in good agreement with the calculated values, which shows the validity of our model predictions. In the past, Shinde *et al.*[46] showed experimentally that 3 monolayers of TMDs vertically stacked in a parallel "AAA configuration" (*i.e.*, 60° folding angle in a trilayer fold) show 9 times SHG enhancement following $I^{SH}_n = I_o n^2$, where n is the number of layers, I^{SH}_n is the resultant SHG intensity of n layers, and I_o is the SHG of 1 layer. Moreover, Mervin Zhao *et al.*[56] reported 9 times SHG enhancement in 3L of 3R MoS_2 (or a 60° folding angle in a trilayer fold) as compared to 1L MoS_2. The phase shifting angle of the folded region is the angular variation in waveform of the folded region with respect to the flat region. This measurement can be important in order to optimize the device performance. We, therefore, calculate the phase shifting angles as follows: (i) $\Delta\varphi_A = \varphi_A - \varphi_{Af}$ and (ii) $\Delta\varphi_B = \varphi_B - \varphi_{Bf}$. A maximum phase shift of 6° is found at 20° and 40° for $\Delta\varphi_B$ and $\Delta\varphi_A$, respectively, as shown in Figure 2f. However, phase shifting angles are too small to be detected accurately within the resolution limit of our experimental setup. An anisotropy response of SHG intensity is expected to be influenced by the folding angle; therefore, we are interested in calculating (linear dichroism (LD))$^{-1} = \rho_B/\rho_A$, which shows a maximum value of 0.3 at 30° θ_f, as shown in Figure 2g. Experimental investigation shows good agreement with the model prediction. The above results thus establish SHG as a powerful technique to monitor folds in atomically thin WS_2.

Strain-dependent SHG studies, in the past,[57,58] were limited to temporary bending methods, which introduce tensile strain temporarily on ultrathin TMDs; however, we have investigated "wrinkles", which are compressive strain induced stable and

https://dx.doi.org/10.1021/acsnano.0c06901
ACS Nano 2020, 14, 15806−15815

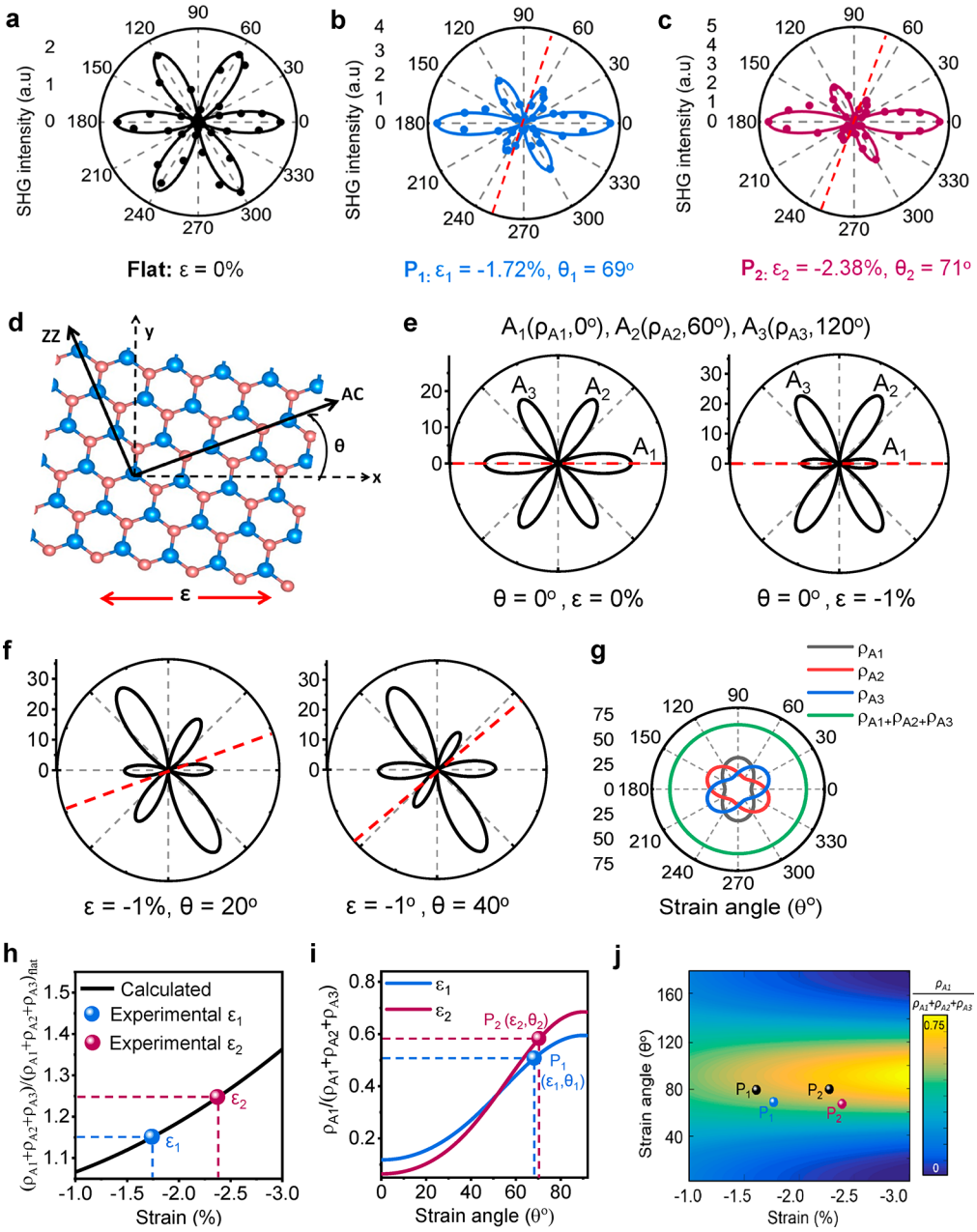

Figure 3. Determination of strain vector by angle-resolved SHG. (a) Experimental investigation of the polarization-resolved SHG intensity $I_{\parallel}(2\omega)$ pattern for (a) flat, (b) P_1 wrinkle, and (c) P_2 wrinkle of 5L WS_2. Continuous lines are the fitted plots, whereas symbols are experimental data points. The red dashed line indicates the direction of strain. Determination of strain amplitude and direction is given in the following figures. (d) Schematic illustration showing the uniaxial strain ε applied along the horizontal direction with a $\theta°$ strain angle between the strain direction and the AC (armchair) direction. Tensile strain and compressive strain are indicated by positive and negative signs, respectively. ZZ: zigzag. (e) Calculated polar response of SHG intensity $I_{\parallel}(2\omega)$ for WS_2 at the strain levels of 0% and −1% (0° strain angle). $A_1(\rho_{A1}, 0°)$, $A_2(\rho_{A2}, 60°)$, and $A_3(\rho_{A3}, 120°)$ are three points with SHG intensity of ρ_{A1}, ρ_{A2}, and ρ_{A3} in the 0°, 60° and 120° direction with respect to the horizontal direction. SHG intensity decreases and increases in the direction along and perpendicular to the compressive strain vector. (f) Calculated SHG $I_{\parallel}(2\omega)$ polar response of WS_2 at strain angles of 20° and 40°($\varepsilon = -1\%$). (g) Calculated strain angle dependent ρ_{A1}, ρ_{A2}, ρ_{A3} and $\rho_{A1}+\rho_{A2}+\rho_{A3}$ ($\varepsilon = -1\%$). (h) Strain-dependent calculated ratio of $\rho_{A1}+\rho_{A2}+\rho_{A3}$ and $(\rho_{A1}+\rho_{A2}+\rho_{A3})_{flat}$, *i.e.*, $(\rho_{A1}+\rho_{A2}+\rho_{A3})/(\rho_{A1}+\rho_{A2}+\rho_{A3})_{flat}$, $\varepsilon_1 = -1.72\%$ (blue sphere) and $\varepsilon_2 = -2.38\%$ (plum sphere) represent two strain values extracted from P_1 and P_2 wrinkles' SHG polar plots shown in Figure 3a–c, where $(\rho_{A1}+\rho_{A2}+\rho_{A3})/(\rho_{A1}+\rho_{A2}+\rho_{A3})_{flat} = 1.15$ and 1.25 for P_1 and P_2. (i) Strain angle ($\theta°$) dependent calculated $\rho_{A1}/(\rho_{A1}+\rho_{A2}+\rho_{A3})$ for ε_1 (blue line) and ε_2 (plum line). $\theta_1 = 69°$ (blue sphere) and $\theta_2 = 71°$ (plum sphere) represent strain angles extracted from P_1 and P_2 SHG polar plots where $\rho_{A1}/(\rho_{A1}+\rho_{A2}+\rho_{A3}) = 0.51$ (P_1) and 0.58 (P_2). (j) SHG contour map showing strain (%) and strain angle ($\theta°$) of P_1 (blue sphere) and P_2 (plum sphere) wrinkles extracted from SHG polar plots solely. The measured strain and strain angle using a combination of AFM and SHG are displayed as black spheres for comparison.

permanent strained nanostructures. In the previous section, we showed that the wrinkles on 5L do not collapse and maintain their wrinkle-like curvature; therefore, the SHG response of wrinkles is expected to be influenced by the local strain vector. In this context, we run polarization-dependent SHG on the flat and winkled regions (P_1 and P_2) of 5L WS_2 (Figure 3a–c) using a

https://dx.doi.org/10.1021/acsnano.0c06901
ACS Nano 2020, 14, 15806−15815

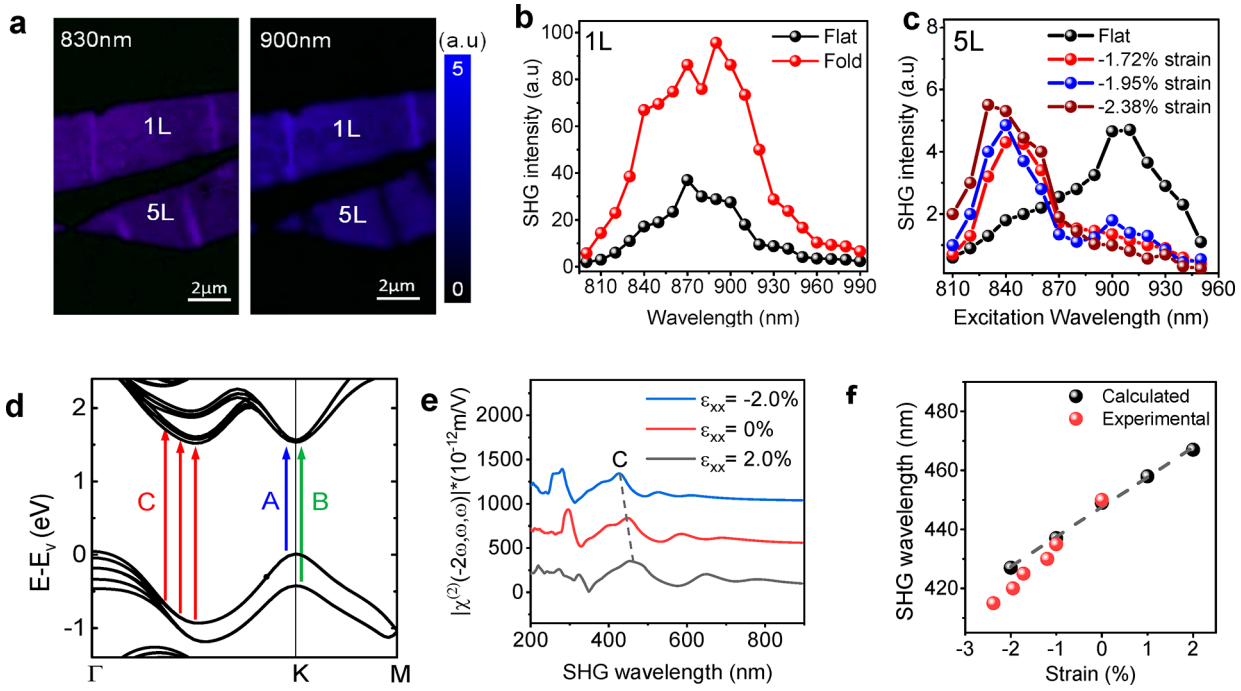

Figure 4. Differentiation of folds and wrinkles through wavelength-dependent SHG. (a) SHG intensity mapping of 1L folds and 5L wrinkles for 830 and 900 nm. 1L folds show an enhancement on both the excitation wavelengths scanned, whereas WS_2 wrinkles show an enhancement and reduction in SHG intensity at 830 and 900 nm, respectively. (b) Excitation wavelength dependent SHG intensity of folded and flat regions of 1L WS_2. Folds show an enhancement at all the wavelengths scanned. (c) Excitation wavelength dependent SHG of flat and strain induced (−1.72%, −1.95%, and −2.38%) wrinkled regions of 5L WS_2. SHG peak blue shifts with the compressive strain. (d) Band structure of 5L WS2 with the label of C calculated by DFT. The arrows indicate the transition in A and B and the band nesting (C). (e) Wavelength-dependent second-order nonlinear susceptibility ($I\chi$) spectra of 5L WS2 for three strain (−2%, 0%, 2%) levels. Spectra are vertically shifted by 500 and 1000 nm for improved visibility. The C-exciton resonance enhanced SHG peak position is indicated by C. (f) Strain-dependent SHG peak wavelength (in resonance with the C exciton). Black color and red color spheres represent calculated and experiments values, respectively. Black dashed line is the linear fit of the calculated values.

pump 830 nm laser, which is initially aligned with the armchair direction of the flat region. Similar to 1L, we get a uniform 6-fold SHG polar pattern from flat 5L WS_2 due to D_{3h} symmetry (Figure 3a).

On the other hand, we get a distortion in the SHG polar pattern on strain-induced wrinkles (*i.e.*, P_1 and P_2 wrinkles) as indicated by spherical dots in Figure 3b,c. In order to understand SHG polar pattern evolution for strain-induced wrinkles, we consider the photoelastic effect, an established approach,[57] for the explanation of SHG polar pattern evolution under strain. Let us take the case of odd-layer WS_2 (D_{3h} symmetry) under uniaxial strain ε along the horizontal direction as depicted in Figure 3d. Strain angle ($\theta°$) is defined as the angle between strain direction and the AC (armchair) direction. The parallel polarized SHG intensity "$I_{\parallel}(2\omega)$" under uniaxial strain ε for D_{3h} symmetry class considering the photoelastic effect is[57]

$$I_{\parallel}(2\omega) \propto \frac{1}{4}(A\cos(3\varphi) + B\cos(2\theta + \varphi))^2 \quad (3)$$

where $A = (1-\nu)(p_1+p_2)(\varepsilon_{xx}+\varepsilon_{yy}) + 2\chi o$ and $B = (1+\nu)(p_1 - p_2)(\varepsilon_{xx}-\varepsilon_{yy})$, p_1 and p_2 are the photoelastic cofficients, ε_{xx} and ε_{yy} are the values of the strain (%) along x and y direction where tensile strain and compressive values are taken as positive and negative respectively, ν is the Poisson ratio, φ is the polarization angle, and χ_0 is the nonlinear susceptibility parameter of the unstrained crystal lattice. Because the wrinkles' formation occurs due to the inward forces (*i.e.*, compressive forces), we will calculate the SHG polar response using the negative amplitude of strain, a Poisson ratio of $\nu_{(WS2)} = 0.22$,[59] $p_1 = 0.75$ nm/V/%,[60] $p_2 = -0.97$ nm/V/%,[60] and $\chi_0 = 4.5$ nm/V.[61] For the first case, parallel polarized SHG intensity "$I_{\parallel}(2w)$" is calculated using a constant strain angle ($\theta = 0°$) and variable strain amplitudes (ε_{xx}) of 0% and −1% using eq 3, and the results are shown in Figure 3e. We have calculated SHG intensity for the range $0° \le \varphi \le 360°$ with a step size of 0.1° polarization angle. SHG quenching and enhancement are found in the direction parallel and perpendicular, respectively, to the strain direction. The quenching and enhancement in their respective directions increase with the strain amplitude. For the second case, SHG intensity is calculated using a constant strain amplitude (ε_{xx}= −1) and variable strain angles of 20° and 40°; the results are shown in Figure 3f. Here, the direction of a pattern's distortion is found to be influenced by the direction of the compressive strain vector, *i.e.*, the strain angle. If $A_1(\rho_{A1}, 0°)$, $A_2(\rho_{A2}, 60°)$, and $A_3(\rho_{A3}, 120°)$ represent three points with SHG intensity of ρ_{A1}, ρ_{A2}, and ρ_{A3} along three AC directions $\varphi = 0°$, 60°, and 120°, respectively (as indicated in Figure 3e), we find that the magnitude of ρ_{A1}, ρ_{A2}, and ρ_{A3} changes with the change in applied strain vector, which is shown in Figure 3e and f. Hereafter, we are interested to find the strain (ε) and strain angle (θ) dependent total SHG intensity. Assuming a constant strain amplitude ($\varepsilon_{xx} = -1$), we have calculated the total SHG intensity ($\rho_{A1}+\rho_{A2}+\rho_{A3}$) for ($0° \le \theta \le 360°$) variable strain angle (θ) with a step size of 0.1°. The results show that the total SHG intensity ($\rho_{A1}+\rho_{A2}+\rho_{A3}$) remains constant for each value of strain angle as shown in Figure 3g. Hereafter, we have calculated compressive strain dependent total SHG intensity ($\rho_{A1}+\rho_{A2}+\rho_{A3}$) for ($0 \le \varepsilon \le -0.06$) with a step size of 0.0001 of ε as shown in Figure S6.

https://dx.doi.org/10.1021/acsnano.0c06901
ACS Nano 2020, 14, 15806−15815

The calculations show that total SHG intensity increases quadratically as compressive strain increases. After finding the individual effect of compressive strain and strain angle on total SHG intensity, we were interested in finding the complete strain vector (strain amplitude and strain angle) and developing a 2D color map to extract the strain amplitude and strain angles of the wrinkles directly from SHG polar plots. Here, we have developed a way as follows: As we know that the total SHG intensity ($\rho_{A1}+\rho_{A2}+\rho_{A3}$) remains constant for each value of strain angle, we can use this finding to calculate strain-dependent $(\rho_{A1}+\rho_{A2}+\rho_{A3})/(\rho_{A1}+\rho_{A2}+\rho_{A3})_{flat}$ with a step size of 0.0001 of ε, which will allow us to extract the single plausible solution values of strain amplitude of P_1 ($\varepsilon_1 = -1.72\%$) and P_2 ($\varepsilon_2 = -2.38\%$) wrinkles directly from SHG polar plots (Figure 3h). Hereafter, we calculate strain angle dependent $\rho_{A1}/(\rho_{A1}+\rho_{A2}+\rho_{A3})$ for ε_1 andε_2 values with a step size of $\theta = 0.1°$ as shown in Figure 3i. The largest value of ρ_{A1} ratio as compared to other counterparts (*i.e.*, ρ_{A2} and ρ_{A3} ratios) tends to provide higher sensitivity and more accurate estimations. Thus, $\theta_1 = 69°$ and $\theta_2 = 71°$are extracted from SHG polar plots of P_1 and P_2 wrinkles, respectively. The extracted values are displayed in a contour plot (Figure 3j). Extracted values of strain angle are very close to each other because the wrinkles (on the same sample) are parallel to each other. The above extracted values of strain amplitude (ε_1 and ε_2 in the *x*-direction) and strain direction (θ_1 and θ_2) fit well to SHG polar plots (Figure 3b,c) using a photoelastic equation (eq 3), which validates our approach. Because our approach only needs SHG intensity at 0°, 60°, and 120°, *i.e.*, ρ_{A1}, ρ_{A2}, and ρ_{A3}, it eliminates the requirement of a time-consuming full SHG polar plot. In order to further validate our model calculations, we use AFM and polarization-dependent SHG to measure the strain $\varepsilon(\%)$ and the strain angle ($\theta°$), respectively, for the selected wrinkles (see Supporting Information Sections S7 and S8 for more details). The measured values (black spheres in Figure 3j) show good agreement with the extracted measurements from SHG polar plots using the scheme given in Figure 3a−i. Conventionally, the strain direction and amplitude measurements require a combination of multiple tools, For instance, AFM, electron microscope, and SHG are required to measure strain angle and amplitude in wrinkles. However, SHG as a single powerful tool has the potential to probe both strain amplitude and strain direction in 2D materials.

SHG response is expected to be influenced by variation in laser wavelength; therefore, we run laser excitation wavelength dependence ($810 \leq \lambda \leq 950$ nm) on the flat, folded, and wrinkled regions of ultrathin WS_2 (Figure 4a−c). Here, we find an SHG peak centered at 870−880 nm laser wavelength (or 435−440 nm of SHG wavelength) in wavelength-dependent SHG for a 1L flat region (Figure 4b). The peak position is attributed to the resonance phenomenon due to the presence of band nesting induced transition (C-peak) (Figure 4d).[48,52,62−66]

The wavelength-dependent SHG response of 1L folds shows SHG enhancement at all the wavelengths scanned (Figure 4b). Recently, SHG is found to be highly sensitive toward strain according to the recent research.[58] This sensitive behavior is shown by significant (49%) SHG quenching per 1% strain in atomically thin $MoSe_2$.[58] Such highly sensitive behavior is also reported for MoS_2.[57] However, no study is reported on the origin of such sensitivity of SHG toward strain in 2D TMDs. Here, we have used wavelength-dependent SHG of strain-induced 5L wrinkles to find the origin of this sensitivity. Wavelength-dependent SHG investigation shows a significant blue shift in SHG peak for 5L wrinkles (Figure 4c). This shift in SHG peak position appears to be dependent on strain amplitude. In the past, Riccardo *et al.*[63] performed biaxial strain dependent reflectance spectra measurements on WS_2 where strain is found to cause a shift of ∼0.07 eV (12 nm) /% strain in the position of C-peak, which is in good agreement with our experimental results (∼15 nm/% compressive strain). In order to further validate, we employed first-principles density functional theory (DFT) using the simulation code Abinit to calculate the strain-dependent wavelength-dependent second-order nonlinear susceptibility $I\chi(-2\omega, \omega, \omega)$ of 5L WS_2 (see Methods section for more details). Tensile strain causes red shifting of the SHG peak, whereas compressive strain results in blue shifting of SHG peak position. The simulation results show a significant shift in SHG peak position (in resonance with the C-exciton) upon strain (%) as shown in Figure 4e,f, which is ∼12.5 nm/strain (%). The experimental measurements show a shift of ∼15 nm/strain (%), which agrees well with the simulation results. Hence, wavelength-dependent SHG clarifies the origin of the resonance-enhanced SHG peak shift in strain-induced wrinkles and thus provides another way to characterize fold and wrinkle nanostructures. Thus, the shift in SHG peak position is attributed to the strain-dependent shift in C-exciton resonance.

CONCLUSIONS

In conclusion, we have shown SHG as a sensitive and powerful tool to investigate the folding angle and strain angle accurately in 2D WS_2. Here, we use a polarization-dependent SHG technique to measure folding angle and strain vector in atomically thin tungsten disulfide (WS_2). Trilayer folds are found to show 9 times SHG enhancement due to the vector superposition of SH wave vectors coming from the individual layers of the fold with 60° folding angle. We find strain-dependent SHG quenching and enhancement in the direction parallel and perpendicular, respectively, to the direction of the compressive strain vector. However, despite a variation in strain angle, total SHG remains constant, which allows us to find the local strain vector using a photoelastic approach. We also demonstrate that band-nesting-induced transition (C peak) can highly enhance SHG, which can be significantly modulated by strain. Our results present an important advance, with applications in nonlinear optical devices.

METHODS

Buckled Sample Fabrication. (i) WS_2 flakes are first exfoliated onto prebuckled gel film using Scotch tape. (ii) Subsequently, the gel film is released, causing compressive forces on exfoliated WS_2 flakes generating well-aligned wrinkles perpendicular to the direction of the compressive forces, which seem to cross the different layered samples. (iii, iv) The wrinkles fall down to form trilayer folds in 1−3L WS_2, whereas higher layered numbers (such as 5L) maintain their wrinkle-like curvature[21] (Figure 1a). Strained WS_2 samples are transferred on a Si/SiO_2/ substrate.[16]

Optical Characterization. SHG measurements are performed on Zeiss 780 confocal microscopy. The fundamental laser field is provided by a tunable pulse Ti:sapphire laser with a pulse width of 150 fs and a repetition rate of 80 MHz. A 50× confocal objective lens (NA = 0.85) is used to excite the sample. SHG measurements are taken at a fundamental laser wavelength of 900 nm. The reflected SH signal is collected by the same objective, separated by a beam splitter, and filtered by suitable optical filters to block the reflected fundamental radiation. The SH character of the detected radiation is verified by its half-wavelength of excitation wavelength (Supporting Information

https://dx.doi.org/10.1021/acsnano.0c06901
ACS Nano 2020, 14, 15806−15815

Section S10) and quadratic power dependence (Supporting Information Section S3) on the pump intensity. A laser with a tunability range (800−1040 nm) is used for wavelength-dependent SHG. For polarization-resolved SHG, an analyzer (polarizer) is used to select the polarization component of the SH radiation parallel to the polarization of the pump beam. The sample is rotated by a rotational stage to obtain the orientation dependence of the SH response.

Simulations. In the present work, the plane-wave method in the framework of DFT using the Abinit code is employed. Local density approximation is used for the exchange−correlation effect, and the energy cutoff of 52 Ry is chosen for the electron wave function expansion. A vacuum layer thicker than 10 Å is included to avoid interaction between periodic layers. The *k*-point sampling is 24 × 24 × 1 for the prime cell of 5L WS_2.

ASSOCIATED CONTENT

Supporting Information

The Supporting Information is available free of charge at https://pubs.acs.org/doi/10.1021/acsnano.0c06901.

Additional data and information regarding strained sample fabrication and folding angle and strain vector determination (PDF)

AUTHOR INFORMATION

Corresponding Author

Yuerui Lu − *Research School of Electrical, Energy and Materials Engineering, College of Engineering and Computer Science, Australian National University, Canberra, ACT 2601, Australia;* orcid.org/0000-0001-6131-3906; Email: yuerui.lu@anu.edu.au

Authors

Ahmed Raza Khan − *Research School of Electrical, Energy and Materials Engineering, College of Engineering and Computer Science, Australian National University, Canberra, ACT 2601, Australia; Department of Industrial and Manufacturing Engineering, University of Engineering and Technology (Rachna College), Lahore 54700, Pakistan;* orcid.org/0000-0002-0962-1861

Boqing Liu − *Research School of Electrical, Energy and Materials Engineering, College of Engineering and Computer Science, Australian National University, Canberra, ACT 2601, Australia*

Tieyu Lü − *Department of Physics and Institute of Theoretical Physics and Astrophysics, Xiamen University, Xiamen 361005, China*

Linglong Zhang − *Research School of Electrical, Energy and Materials Engineering, College of Engineering and Computer Science, Australian National University, Canberra, ACT 2601, Australia*

Ankur Sharma − *Research School of Electrical, Energy and Materials Engineering, College of Engineering and Computer Science, Australian National University, Canberra, ACT 2601, Australia;* orcid.org/0000-0002-0863-1857

Yi Zhu − *Research School of Electrical, Energy and Materials Engineering, College of Engineering and Computer Science, Australian National University, Canberra, ACT 2601, Australia*

Wendi Ma − *Research School of Electrical, Energy and Materials Engineering, College of Engineering and Computer Science, Australian National University, Canberra, ACT 2601, Australia*

Complete contact information is available at: https://pubs.acs.org/10.1021/acsnano.0c06901

Author Contributions

Y.L. conceived and supervised the project; A.K. and W.M prepared strained samples; A.K., B.L., and A.S. carried out all the SHG measurements; A.K. and Y.L. analyzed the data; A.K. carried out model calculations; L.Z. and B. L. obtained the AFM imaging; A.K., W.M., and Y.Z. helped with the schematic preparation; A.K. and Y.L. drafted the manuscript; and all authors contributed to the manuscript.

Notes

The authors declare no competing financial interest.

ACKNOWLEDGMENTS

We acknowledge the support from the ANU Ph.D. student scholarship, China Scholarship Council, Australian Research Council (ARC; numbers DE140100805 and DP180103238), and Australian National Heart Foundation (ARIES ID: 35852). We would also like to thank Mr. D. Webb from Center of Advanced Microscopy (CAM), Australian National University.

REFERENCES

(1) Mak, K. F.; Shan, J. Photonics and Optoelectronics of 2D Semiconductor Transition Metal Dichalcogenides. *Nat. Photonics* **2016**, *10*, 216−226.

(2) Wang, G.; Chernikov, A.; Glazov, M. M.; Heinz, T. F.; Marie, X.; Amand, T.; Urbaszek, B. Colloquium: Excitons in Atomically Thin Transition Metal Dichalcogenides. *Rev. Mod. Phys.* **2018**, *90*, 021001.

(3) Han, X.; Morgan Stewart, H.; Shevlin, S. A.; Catlow, C. R. A.; Guo, Z. X. Strain and Orientation Modulated Bandgaps and Effective Masses of Phosphorene Nanoribbons. *Nano Lett.* **2014**, *14*, 4607−4614.

(4) Sharma, A.; Khan, A. R.; Zhu, Y.; Halbich, R.; Ma, W.; Tang, Y.; Wang, B.; Lu, Y. Quasi-Line Spectral Emissions from Highly Crystalline One-Dimensional Organic Nanowires. *Nano Lett.* **2019**, *19*, 7877−7886.

(5) Zhu, Y.; Yang, J.; Zhang, S.; Mokhtar, S.; Pei, J.; Wang, X.; Lu, Y. Strongly Enhanced Photoluminescence in Nanostructured Monolayer MoS 2 by Chemical Vapor Deposition. *Nanotechnology* **2016**, *27*, 135706.

(6) Sohler, W.; Hu, H.; Ricken, R.; Quiring, V.; Vannahme, C.; Herrmann, H.; Büchter, D.; Reza, S.; Grundkötter, W.; Orlov, S. Integrated Optical Devices in Lithium Niobate. *Opt. Photonics News* **2008**, *19*, 24.

(7) Cho, K.; Yang, J.; Lu, Y. Phosphorene: An Emerging 2D Material. *J. Mater. Res.* **2017**, *32*, 2839−2847.

(8) Zhang, L.; Yan, H.; Sun, X.; Dong, M.; Yildirim, T.; Wang, B.; Wen, B.; Neupane, G. P.; Sharma, A.; Zhu, Y. Modulated Interlayer Charge Transfer Dynamics in a Monolayer TMD/Metal Junction. *Nanoscale* **2019**, *11*, 418−425.

(9) Sharma, A.; Zhang, L.; Tollerud, J. O.; Dong, M.; Zhu, Y.; Halbich, R.; Vogl, T.; Liang, K.; Nguyen, H. T.; Wang, F. Supertransport of Excitons in Atomically Thin Organic Semiconductors at the 2D Quantum Limit. *Light: Sci. Appl.* **2020**, *9*, 116.

(10) Sharma, A.; Wen, B.; Liu, B.; Myint, Y. W.; Zhang, H.; Lu, Y. Defect Engineering in Few-Layer Phosphorene. *Small* **2018**, *14*, 1704556.

(11) Blundo, E.; Felici, M.; Yildirim, T.; Pettinari, G.; Tedeschi, D.; Miriametro, A.; Liu, B.; Ma, W.; Lu, Y.; Polimeni, A. Evidence of the Direct-to-Indirect Band Gap Transition in Strained Two-Dimensional WS_2, MoS_2, and WSe_2. *Phys. Rev. Res.* **2020**, *2*, 12024.

(12) Santos, E. J. G.; Kaxiras, E. Electrically Driven Tuning of the Dielectric Constant in MoS_2 Layers. *ACS Nano* **2013**, *7*, 10741−10746.

(13) Pei, J.; Yang, J.; Xu, R.; Zeng, Y. H.; Myint, Y. W.; Zhang, S.; Zheng, J. C.; Qin, Q.; Wang, X.; Jiang, W. Exciton and Trion Dynamics in Bilayer MoS2. *Small* **2015**, *11*, 6384−6390.

(14) Zhu, Y.; Li, Z.; Zhang, L.; Wang, B.; Luo, Z.; Long, J.; Yang, J.; Fu, L.; Lu, Y. High-Efficiency Monolayer Molybdenum Ditelluride Light-Emitting Diode and Photodetector. *ACS Appl. Mater. Interfaces* **2018**, *10*, 43291−43298.
(15) Lu, J.; Yang, J.; Carvalho, A.; Liu, H.; Lu, Y.; Sow, C. H. Light-Matter Interactions in Phosphorene. *Acc. Chem. Res.* **2016**, *49*, 1806−1815.
(16) Xu, R.; Yang, J.; Zhu, Y.; Yan, H.; Pei, J.; Myint, Y. W.; Zhang, S.; Lu, Y. Layer-Dependent Surface Potential of Phosphorene and Anisotropic/Layer-Dependent Charge Transfer in Phosphorene-Gold Hybrid Systems. *Nanoscale* **2016**, *8*, 129−135.
(17) Pei, J.; Yang, J.; Yildirim, T.; Zhang, H.; Lu, Y. Many-Body Complexes in 2D Semiconductors. *Adv. Mater.* **2019**, *31*, 1706945.
(18) Neupane, G. P.; Zhang, L.; Yildirim, T.; Zhou, K.; Wang, B.; Tang, Y.; Ma, W.; Xue, Y.; Lu, Y. A Prospective Future towards Bio/Medical Technology and Bioelectronics Based on 2D VdWs Heterostructures. *Nano Res.* **2020**, *13*, 1−17.
(19) Wen, B.; Zhu, Y.; Yudistira, D.; Boes, A.; Zhang, L.; Yidirim, T.; Liu, B.; Yan, H.; Sun, X.; Zhou, Y. Ferroelectric-Driven Exciton and Trion Modulation in Monolayer Molybdenum and Tungsten Diselenides. *ACS Nano* **2019**, *13*, 5335−5343.
(20) Vogl, T.; Doherty, M. W.; Buchler, B. C.; Lu, Y.; Lam, P. K. Atomic Localization of Quantum Emitters in Multilayer Hexagonal Boron Nitride. *Nanoscale* **2019**, *11*, 14362−14371.
(21) Castellanos-Gomez, A.; Roldán, R.; Cappelluti, E.; Buscema, M.; Guinea, F.; Van Der Zant, H. S. J.; Steele, G. A. Local Strain Engineering in Atomically Thin MoS_2. *Nano Lett.* **2013**, *23*, 534.
(22) Tedeschi, D.; Blundo, E.; Felici, M.; Pettinari, G.; Liu, B.; Yildrim, T.; Petroni, E.; Zhang, C.; Zhu, Y.; Sennato, S. Controlled Micro/Nanodome Formation in Proton-Irradiated Bulk Transition-Metal Dichalcogenides. *Adv. Mater.* **2019**, *31*, 1903795.
(23) Blundo, E.; Di Giorgio, C.; Pettinari, G.; Yildirim, T.; Felici, M.; Lu, Y.; Bobba, F.; Polimeni, A. Engineered Creation of Periodic Giant, Nonuniform Strains in MoS_2 Monolayers. *Adv. Mater. Interfaces* **2020**, *7*, 2000621.
(24) Pei, J.; Gai, X.; Yang, J.; Wang, X.; Yu, Z.; Choi, D.-Y.; Luther-Davies, B.; Lu, Y. Producing Air-Stable Monolayers of Phosphorene and Their Defect Engineering. *Nat. Commun.* **2016**, *7*, 10450.
(25) Du, Y.; Liu, H.; Neal, A. T.; Si, M.; Ye, P. D. Molecular Doping of Multilayer MoS_2 Field-Effect Transistors: Reduction in Sheet and Contact Resistances. *IEEE Electron Device Lett.* **2013**, *34*, 1328−1330.
(26) Fujisawa, K.; Komiyama, K.; Muramatsu, H.; Shimamoto, D.; Tojo, T.; Kim, Y. A.; Hayashi, T.; Endo, M.; Oshida, K.; Terrones, M.; Dresselhaus, M. Chirality-Dependent Transport in Double-Walled Carbon Nanotube Assemblies: The Role of Inner Tubes. *ACS Nano* **2011**, *5*, 7547−7554.
(27) Jena, P. V.; Galassi, T. V.; Roxbury, D.; Heller, D. A. Review—Progress toward Applications of Carbon Nanotube Photoluminescence. *ECS J. Solid State Sci. Technol.* **2017**, *6*, M3075−M3077.
(28) Simien, D.; Fagan, J. A.; Luo, W.; Douglas, J. F.; Migler, K.; Obrzut, J. Influence of Nanotube Length on the Optical and Conductivity Properties of Thin Single-Wall Carbon Nanotube Networks. *ACS Nano* **2008**, *2*, 1879−1884.
(29) Choi, J. H. J.; Zhang, H.; Choi, J. H. J. Modulating Optoelectronic Properties of Two-Dimensional Transition Metal Dichalcogenide Semiconductors by Photoinduced Charge Transfer. *ACS Nano* **2016**, *10*, 1671−1680.
(30) Du, L.; Yu, H.; Liao, M.; Wang, S.; Xie, L.; Lu, X.; Zhu, J.; Li, N.; Shen, C.; Chen, P.; Yang, R.; Shi, D.; Zhang, G. Modulating PL and Electronic Structures of MoS_2/ Graphene Heterostructures *via* Interlayer Twisting Angle. *Appl. Phys. Lett.* **2017**, *111*, 263106.
(31) Choi, W.; Akhtar, I.; Rehman, M. A.; Kim, M.; Kang, D.; Jung, J.; Myung, Y.; Kim, J.; Cheong, H.; Seo, Y. Twist-Angle-Dependent Optoelectronics in a Few-Layer Transition-Metal Dichalcogenide Heterostructure. *ACS Appl. Mater. Interfaces* **2019**, *11*, 2470−2478.
(32) Wang, Y.; Cong, C.; Yang, W.; Shang, J.; Peimyoo, N.; Chen, Y.; Kang, J.; Wang, J.; Huang, W.; Yu, T. Strain-Induced Direct-Indirect Bandgap Transition and Phonon Modulation in Monolayer WS 2. *Nano Res.* **2015**, *8*, 2562−2572.
(33) Khan, A. R.; Lu, T.; Ma, W.; Lu, Y.; Liu, Y. Tunable Optoelectronic Properties of WS_2 by Local Strain Engineering and Folding. *Adv. Electron. Mater.* **2020**, *6*, 1901381.
(34) Castellanos-Gomez, A.; van der Zant, H. S. J.; Steele, G. A. Folded MoS_2 Layers with Reduced Interlayer Coupling. *Nano Res.* **2014**, *7*, 572−578.
(35) Amorim, B.; Cortijo, A.; de Juan, F.; Grushin, A. G.; Guinea, F.; Gutiérrez-Rubio, A.; Ochoa, H.; Parente, V.; Roldán, R.; San-Jose, P.; Schiefele, J.; Sturla, M.; Vozmediano, M. A. H. Novel Effects of Strains in Graphene and Other Two Dimensional Materials. *Phys. Rep.* **2016**, *617*, 1−54.
(36) Liu, J.; Sun, X.; Pan, D.; Wang, X.; Kimerling, L. C.; Koch, T. L.; Michel, J. Tensile-Strained, *n*-Type Ge as a Gain Medium for Monolithic Laser Integration on Si. *Opt. Express* **2007**, *15*, 11272.
(37) Roldán, R.; Castellanos-Gomez, A.; Cappelluti, E.; Guinea, F. Strain Engineering in Semiconducting Two-Dimensional Crystals. *J. Phys.: Condens. Matter* **2015**, *27*, 313201.
(38) Dhakal, K. P.; Roy, S.; Jang, H.; Chen, X.; Yun, W. S.; Kim, H.; Lee, J.; Kim, J.; Ahn, J. H. Local Strain Induced Band Gap Modulation and Photoluminescence Enhancement of Multilayer Transition Metal Dichalcogenides. *Chem. Mater.* **2017**, *29*, 5124−5133.
(39) Chai, Y.; Su, S.; Yan, D.; Ozkan, M.; Lake, R.; Ozkan, C. S. Strain Gated Bilayer Molybdenum Disulfide Field Effect Transistor with Edge Contacts. *Sci. Rep.* **2017**, *7*, 41593.
(40) Shen, T.; Penumatcha, A. V.; Appenzeller, J. Strain Engineering for Transition Metal Dichalcogenides Based Field Effect Transistors. *ACS Nano* **2016**, *10*, 4712−4718.
(41) Quereda, J.; Palacios, J. J.; Agräit, N.; Castellanos-Gomez, A.; Rubio-Bollinger, G. Strain Engineering of Schottky Barriers in Single- and Few-Layer MoS_2 Vertical Devices. *2D Mater.* **2017**, *4*, 021006.
(42) Robinson, B. J.; Giusca, C. E.; Gonzalez, Y. T.; Kay, N. D.; Kazakova, O.; Kolosov, O. V. Structural, Optical and Electrostatic Properties of Single and Few-Layers MoS_2: Effect of Substrate. *2D Mater.* **2015**, *2*, 015005.
(43) Desai, S. B.; Seol, G.; Kang, J. S.; Fang, H.; Battaglia, C.; Kapadia, R.; Ager, J. W.; Guo, J.; Javey, A. Strain-Induced Indirect to Direct Bandgap Transition in Multilayer WSe_2. *Nano Lett.* **2014**, *14*, 4592−4597.
(44) Liu, Z.; Amani, M.; Najmaei, S.; Xu, Q.; Zou, X.; Zhou, W.; Yu, T.; Qiu, C.; Birdwell, A. G.; Crowne, F. J.; Vajtai, R.; Yakobson, B. I.; Xia, Z.; Dubey, M.; Ajayan, P. M.; Lou, J. Strain and Structure Heterogeneity in MoS_2 Atomic Layers Grown by Chemical Vapour Deposition. *Nat. Commun.* **2014**, *5*, 5246.
(45) Hsu, W.-T.; Zhao, Z.-A.; Li, L.-J.; Chen, C.-H.; Chiu, M.-H.; Chang, P.-S.; Chou, Y.-C.; Chang, W.-H. Second Harmonic Generation from Artificially Stacked Transition Metal Dichalcogenide Twisted Bilayers. *ACS Nano* **2014**, *8*, 2951−2958.
(46) Shinde, S. M.; Dhakal, K. P.; Chen, X.; Yun, W. S.; Lee, J.; Kim, H.; Ahn, J.-H. Stacking-Controllable Interlayer Coupling and Symmetric Configuration of Multilayered MoS_2. *NPG Asia Mater.* **2018**, *10*, No. e468-e468.
(47) Wang, H.; Qian, X. Giant Optical Second Harmonic Generation in Two-Dimensional Multiferroics. *Nano Lett.* **2017**, *17*, 5027−5034.
(48) Li, Y.; Rao, Y.; Mak, K. F.; You, Y.; Wang, S.; Dean, C. R.; Heinz, T. F. Probing Symmetry Properties of Few-Layer MoS_2 and h-BN by Optical Second-Harmonic Generation. *Nano Lett.* **2013**, *13*, 3329−3333.
(49) Pei, J.; Yang, J.; Xu, R.; Zeng, Y. H.; Myint, Y. W.; Zhang, S.; Zheng, J. C.; Qin, Q.; Wang, X.; Jiang, W.; Lu, Y. Exciton and Trion Dynamics in Bilayer MoS_2. *Small* **2015**, *11*, 6384−6390.
(50) Kuriakose, S.; Ahmed, T.; Taylor, P.; Zhu, Y.; Spencer, M. J. S.; Balendhran, S.; Lu, Y.; Bansal, V.; Sriram, S.; Bhaskaran, M.; Walia, S. Generating Strong Room-Temperature Photoluminescence in Black Phosphorus Using Organic Molecules. *2D Mater.* **2019**, *6*, 015009.
(51) Khan, A. R.; Liu, B.; Zhang, L.; Zhu, Y.; He, X.; Zhang, L.; Lü, T.; Lu, Y. Extraordinary Temperature Dependent Second Harmonic Generation in Atomically Thin Layers of Transition-Metal Dichalcogenides. *Adv. Opt. Mater.* **2020**, *8*, 2000441.

https://dx.doi.org/10.1021/acsnano.0c06901
ACS Nano 2020, 14, 15806−15815

(52) Malard, L. M.; Alencar, T. V.; Barboza, A. P. M.; Mak, K. F.; De Paula, A. M. Observation of Intense Second Harmonic Generation from MoS_2 Atomic Crystals. *Phys. Rev. B: Condens. Matter Mater. Phys.* **2013**, *87*, 1−5.
(53) Le, C. T.; Clark, D. J.; Ullah, F.; Senthilkumar, V.; Jang, J. I.; Sim, Y.; Seong, M. J.; Chung, K. H.; Park, H.; Kim, Y. S. Nonlinear Optical Characteristics of Monolayer $MoSe_2$. *Ann. Phys.* **2016**, *528*, 551−559.
(54) Shi, J.; Yu, P.; Liu, F.; He, P.; Wang, R.; Qin, L.; Zhou, J.; Li, X.; Zhou, J.; Sui, X.; Zhang, S.; Zhang, Y.; Zhang, Q.; Sum, T. C.; Qiu, X.; Liu, Z.; Liu, X. 3R MoS_2 with Broken Inversion Symmetry: A Promising Ultrathin Nonlinear Optical Device. *Adv. Mater.* **2017**, *29*, 1701486.
(55) Zhang, Y.; Zhang, Y.; Ji, Q.; Ju, J.; Yuan, H.; Shi, J.; Gao, T.; Ma, D.; Liu, M.; Chen, Y.; Song, X.; Hwang, H. Y.; Cui, Y.; Liu, Z. Controlled Growth of High-Quality Monolayer WS_2 Layers on Sapphire and Imaging Its Grain Boundary. *ACS Nano* **2013**, *7*, 8963−8971.
(56) Zhao, M.; Ye, Z.; Suzuki, R.; Ye, Y.; Zhu, H.; Xiao, J.; Wang, Y.; Iwasa, Y.; Zhang, X. Atomically Phase-Matched Second-Harmonic Generation in a 2D Crystal. *Light: Sci. Appl.* **2016**, *5*, No. e16131.
(57) Mennel, L.; Furchi, M. M.; Wachter, S.; Paur, M.; Polyushkin, D. K.; Mueller, T. Optical Imaging of Strain in Two-Dimensional Crystals. *Nat. Commun.* **2018**, *9*, 516.
(58) Liang, J.; Zhang, J.; Li, Z.; Hong, H.; Wang, J.; Zhang, Z.; Zhou, X.; Qiao, R.; Xu, J.; Gao, P.; Liu, Z.; Sun, Z.; Meng, S.; Liu, K.; Yu, D. Monitoring Local Strain Vector in Atomic-Layered $MoSe_2$ by Second-Harmonic Generation. *Nano Lett.* **2017**, *17*, 7539−7543.
(59) Liu, K.; Yan, Q.; Chen, M.; Fan, W.; Sun, Y.; Suh, J.; Fu, D.; Lee, S.; Zhou, J.; Tongay, S.; Ji, J.; Neaton, J. B.; Wu, J. Elastic Properties of Chemical-Vapor-Deposited Monolayer MoS_2, WS_2 and Their Bilayer Heterostructures. *Nano Lett.* **2014**, *14*, 5097−5103.
(60) Mennel, L.; Paur, M.; Mueller, T. Second Harmonic Generation in Strained Transition Metal Dichalcogenide Monolayers: MoS_2, $MoSe_2$, WS_2, and WSe_2. *APL Photonics* **2019**, *4*, 034404.
(61) Janisch, C.; Wang, Y.; Ma, D.; Mehta, N.; Elías, A. L.; Perea-López, N.; Terrones, M.; Crespi, V.; Liu, Z. Extraordinary Second Harmonic Generation in Tungsten Disulfide Monolayers. *Sci. Rep.* **2015**, *4*, 1−5.
(62) Zhu, B.; Chen, X.; Cui, X. Exciton Binding Energy of Monolayer WS2. *Sci. Rep.* **2015**, *5*, 9218.
(63) Frisenda, R.; Drüppel, M.; Schmidt, R.; Michaelis de Vasconcellos, S.; Perez de Lara, D.; Bratschitsch, R.; Rohlfing, M.; Castellanos-Gomez, A. Biaxial Strain Tuning of the Optical Properties of Single-Layer Transition Metal Dichalcogenides. *npj 2D Mater. Appl.* **2017**, *1*, 10.
(64) Kikuchi, Y.; Miyauchi, Y.; Takaoka, R.; Suzuki, T.; Tanaka, M.; Ohno, S. Multiple-Peak Resonance of Optical Second Harmonic Generation Arising from Band Nesting in Monolayer Transition Metal Dichalcogenides and the Fine Structure of the Exciton. *Phys. Rev. B: Condens. Matter Mater. Phys.* **2019**, *100*, 075301.
(65) Beach, K.; Lucking, M. C.; Terrones, H. Strain Dependence of Second Harmonic Generation in Transition Metal Dichalcogenide Monolayers and the Fine Structure of the Exciton. *Phys. Rev. B: Condens. Matter Mater. Phys.* **2020**, *101*, 155431.
(66) Niu, Y.; Gonzalez-Abad, S.; Frisenda, R.; Marauhn, P.; Drüppel, M.; Gant, P.; Schmidt, R.; Taghavi, N.; Barcons, D.; Molina-Mendoza, A.; de Vasconcellos, S.; Bratschitsch, R.; Perez, D. L.; David, R.; Castellanos-Gomez, A. Thickness-Dependent Differential Reflectance Spectra of Monolayer and Few-Layer MoS_2, $MoSe_2$, WS_2 and WSe_2. *Nanomaterials* **2018**, *8*, 725.

https://dx.doi.org/10.1021/acsnano.0c06901
ACS Nano 2020, 14, 15806−15815